J. Appl. Comput. Mech., 12(3) (2026) 866-878
DOI: 10.22055/jacm.2025.48524.5295

ISSN: 2383-4536
jacm.scu.ac.ir

Shahid Chamran University of Ahvaz

Journal of Applied and Computational Mechanics

Research Paper

Effects of Dimples as Vortex Cavities on the Aerodynamic Performance of Darrieus Vertical Axis Wind Turbine

Yuewen Huang[1], Lidong Zhang[1], Changpeng Song[1], Guoqiang Tong[2], Yuze Zhao[3], Tieliu Jiang[1], Xin Meng[4]

[1] School of Energy and Power Engineering, Northeast Electric Power University, No. 169, Changchun Road Sub-district, Jilin City, Jilin Province, 132012, China, Email: YuewenHuang1821@163.com (Y.H.); nedu1015@aliyun.com (L.Z.); 2202400614@neepu.edu.cn (C.S.); jiangtieliu@163.com (T.J.)

[2] School of Aerospace Engineering, Nanjing University of Aeronautics and Astronautics, Jiangjun Road No.29, Nanjing City, 211106, China, Email: guoqiangtong@nuaa.edu.cn

[3] School of Electrical Automation and Information Engineering, Tianjin University, No. 92, Weijin Road, Nankai District, Tianjin City, 300072, China, Email: yuzezhao@tju.edu.cn

[4] Huaneng Jilin Power Generation CO, LTD., Xinghuo Road No.399, High-tech Development Zone, Changchun City,130012, China, Email: linglei@263.net

Received June 11 2025; Revised September 15 2025; Accepted for publication October 09 2025.
✉ Corresponding author: G. Tong (guoqiangtong@nuaa.edu.cn)

Abstract. This paper investigates the aerodynamic performance enhancement of a Straight-Bladed Vertical Axis Wind Turbine (VAWT) through dimple optimization. This study employs Orthogonal Experimental Design (OED), a classical Design of Experiments (DoE) methodology, to systematically analyze dimple parameters. Initially, three key single-dimple parameters (diameter, position, depth) were investigated, followed by an extended Dual-dimple configuration incorporating six parameters (x/c, d_1, l_1, d_2, l_2, s). The OED approach achieves optimization of these multi-factor, multi-level systems with minimal computational cost by scientifically selecting representative combinations from full factorial experiments. Numerical simulations using the Transition SST turbulence model demonstrated that the optimal Dual-dimple design improved the pressure coefficient (C_{pe}) by 114.9% and the C_p of the optimal Dual-dimple airfoil is 0.1227 for the numerical simulation at a Tip Speed Ratio (*TSR*) of 3. The position x/c of dimple 1, with an F_{value} of 2.729, was identified as the most influential parameter, exceeding the significance threshold of 2.25. The design effectively delayed dynamic stall and suppressed boundary layer separation, though performance gains diminished with additional dimples or higher *TSR* values. These findings provide valuable insights for optimizing VAWT blade design through surface modifications.

Keywords: Wind turbine; Dimple; OED; Dynamic stall; Numerical simulation.

1. Introduction

With the development of human beings, fossil energy began to run out. As a kind of clean and renewable energy, wind energy has been widely used in recent year [1], and many wind power facilities such as offshore wind farms have been built [2] Wind turbines are divided into vertical-axis wind turbines (VAWTs) and Horizontal-Axis Wind Turbines (HAWTs) [3]. Compared with HAWTs, the most obvious advantages of VAWTs are that their operating conditions are relatively loose, and VAWTs can make full use of the unstable wind whose direction changes frequently around the city [4].

VAWTs are mainly divided into two types: Savonius and Darrieus [5-8]. The Savonius wind turbine is a promising type of wind turbine at low wind speeds, but its efficiency is low [9]. The Darrieus wind turbine has better aerodynamic performance than the Savonius wind turbine. With the growing attention to VAWTs, more and more researchers have begun to study how to improve the efficiency of VAWTs and expand their application. Although the wind tunnel experiment is ideal in the research, the development of the wind tunnel has limitations due to the construction of the wind tunnel and the cost to wind turbine manufacturing. Therefore, the development of numerical simulation is a fine complement for the wind tunnel experiment [10].

Several papers about VAWTs based on numerical simulation have been published. For example, Shi et al. [11] placed an oscillating micro-cylinder on upstream of the S809 airfoil to investigate the aerodynamic performance using numerical simulation. Rezaeiha et al. [12] studied the influence of operating parameters such as tip speed ratio, Reynolds number and turbulence intensity) on the performance of VAWTs based on CFD. Zuo et al. [13] performed unsteady numerical simulations to investigate the wake structure of a three-bladed H-type VAWT and its influence on the aerodynamic performance. On the one hand, Zhang et al. [14] investigated the influence of blade curvature and thickness on power coefficient. It was found that symmetric airfoils are better than asymmetric airfoils under the same operating conditions. On the other hand, as the thickness of the blade increases, the power coefficient shows a trend that it increases at first and then drops at a certain pitch angle. Furthermore, many researchers have investigated the aerodynamic performance and vortex structure of Straight-Bladed (SB) [15-17]. For example, Jiang et al. [18] studied the influence of vortex generators on wind turbine aerodynamic performance. Li et al. [10, 19] investigated the power

Published online: October 16 2025

performance and wake characteristics of a SB-VAWT with field experiments. Zhen et al. [20] proposed a Variable-Pitch (VP) technology to focus on the aerodynamics improvement a small angle of attack. Besides, Li et al. [21] proposed an innovative truncated-cone-shaped Wind Gathering Device (WGD) to improve the starting performance of the SB-VAWT. The results revealed that the WGD is effective for both the static and dynamic performance of SB-VAWT. Chen et al. [22] presented a novel multi-objective optimization algorithm for VAWT whose results showed that this algorithm has good performance in handling the multi-objective optimization of VAWT. Zhang et al. [23] investigated the effects of sinusoidal leading-edge protuberances at a low Re of 5.0×10^4. The results indicated that the sinusoidal protuberances effectively delayed the dynamic stall, but the corresponding aerodynamic performance was impaired.

To improve the efficiency of VAWT, the researchers added a piece of additional auxiliary equipment on the blade. Almohammadi [24] investigated the influence of the trailing edge profile on the performance of SB-VAWT. They discovered that the thickness of the blade plays an important role in improving the aerodynamic performance at a relatively low tip speed ratio. And when the tip speed ratio is higher than 1.75, the circular trailing edge has a very significant effect on improving the performance of VAWT. Zhang et al. [25] used the Orthogonal Experiment Design (OED) method to numerically simulate a two-blade H-shaped VAWT with a winglet. The results indicated that the winglet is effective in decreasing the tip vortex in the aerospace field. Li et al. [26] installed a truncated-cone-shaped WGD at the top and bottom of SB-VAWT to increase the wind speed. Ali et al. [27] noted that recent advancements in passive flow control for Darrieus VAWTs include Gurney flaps to enhance lift at low TSRs, vortex generators for boundary layer mixing, and bio-inspired leading-edge serrations to delay dynamic stall. Additionally, dimples on blade surfaces have shown promise in trapping vortices and improving efficiency, while adaptive flaps mimic avian feather mechanics to suppress separation. Jiang et al. [28] proposed a novel VAWT system to obtain the fluid mechanical details using CFD simulation. The system consisted of two contra-rotating VAWT rotors and a deflector that is placed between the two rotors. It was found that the deflection plate increased the velocity of the partial fluid and significantly affected the output power of the two rotors. Fang et al. [29] proposed a Lift-Drag Combined Starter (LDCS) optimize the starting characteristics of lift-type VAWT. The results demonstrated that the static torque coefficient of LDCS increased significantly with the increased incoming wind speed. The above studies have achieved good improvement in the aerodynamic performance of VAWT. Recently, some scholars added a dimple on the blade to enhance efficiency and relieve the occurrence of dynamic stall. Sobhani et al. [30] analyzed a two-dimensional H-Darrieus wind turbine and pointed out that adding a dimple on the pressure surface of the blade could improve the aerodynamic characteristics. The improvement of circular dimples was better than those of triangular or rectangular ones. Among all types of dimples, a dimple with a larger radius and closed position to the leading edge of the blade obtains the best improvement in performance. But adding dimple on the suction surface of the blade could only improve its performance at high tip speed ratios. Yue et al. [31] investigated the effects of groove characteristics on aerodynamic behavior. The indented groove eliminates laminar separation bubbles and also has the potential to improve the aerodynamic performance of the VAWT. Miladi [32] created a single dimple on the upper surface of the trailing edge of the airfoil, namely the UST airfoil. The results demonstrated that the UST airfoil obtains an improvement of 18% for power coefficient at a tip speed ratio of 3.5. They also created an airfoil with Dual-dimple on different positions of the blades. And it is found that the Dual-dimple airfoil on an upper and lower surface (trailing edge) has the highest power coefficient (C_P) value of 0.34, indicating a maximum improvement of 10% compared to the smooth airfoil.

The above studies have demonstrated that dimple-based designs, such as dimples and trapped vortex cavities, can enhance VAWT performance, but critical gaps remain. Specifically, prior works primarily focus on single-dimple configurations [33] or active suction methods [34], with limited exploration of passive multi-dimple designs and their systematic parameter optimization. Additionally, there is a lack of in-depth analysis on the influence of key dimple parameters on the power coefficient—particularly for dual-dimple airfoils—and the underlying aerodynamic mechanisms [32]. Notably, the effect of increasing the number of cavities on performance, a crucial aspect of multi-dimple design scalability, has not been adequately addressed in existing research.

To address these gaps, this study proposes a dual-dimple airfoil model optimized using the Orthogonal Experimental Design (OED) method; through comprehensive parameter analysis, the model systematically evaluates six dimple design parameters and identifies the position of the first dimple as the most influential factor—a novel finding that has not been quantified before, which precisely fills the gap in systematic parameter optimization highlighted earlier. The structure of the paper is as follows: Section 2 elaborates on the physical and numerical models. Section 3 applies OED to optimize the dimple parameters. Section 4 clarifies the performance-enhancing mechanisms by comparing the flow fields of the dual-dimple airfoil and the smooth airfoil. Section 5 summarizes the research and puts forward design recommendations, with the findings of this study aiming to bridge the gap between empirical dimple designs and systematic optimization in Vertical Axis Wind Turbines (VAWTs).

2. Physical and Numerical Model

2.1. Physical model introduction

This study adopts the test model in the wind tunnel experiment of Danao [35] at the University of Sheffield. The test is based on a symmetrical NACA0022 with a fine performance. The relevant parameters are shown in Table 1 below and the computational domain for a three-bladed VAWT is shown in Fig. 1.

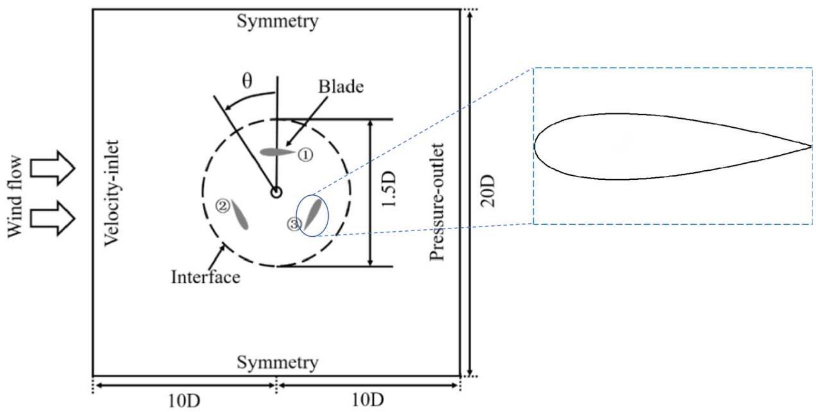

Fig. 1. Domain dimensions and boundary conditions.

Table 1. Rotor and blade geometric parameters.

Parameter	Symbol	Value
Solidity	σ	0.34
Blade chord length	c	0.04 m
Rotor diameter	D	0.7 m
Diameter of the center tower	ds	0.027 m

2.2. Numerical simulation method

2.2.1. Governing equations and turbulence models

In this research work, commercial software ANSYS Fluent was used for simulation analysis. A stable two-dimensional numerical simulation was conducted using the Unsteady Reynolds-Averaged Navier-Stokes (URANS) method. The URANS equation is used to describe the fluid flow dynamics near the blade, which facilitates a comprehensive and accurate analysis of the unsteady turbulent fluid flow behavior. The formulation of the URANS equations for Newtonian incompressible flow relies on the assumption of a constant density that does not fluctuate with pressure. This method is applicable when the tip tangential velocity is kept below Mach 0.3. This reinforces the underlying assumption of incompressibility in the flow analysis presented in this paper. The URANS equations for incompressible flow are as follows [36]:

The governing equation is as follows:

1. Mass conservation equation:

$$\frac{\partial u_i}{\partial x_i} = 0 \tag{1}$$

2. Momentum conservation equation:

$$\frac{\partial u_i}{\partial t} + u_j \frac{\partial u_i}{\partial x_j} = -\frac{1}{\rho}\frac{\partial p}{\partial x_i} + \nu \frac{\partial^2 u_i}{\partial x_j \partial x_j} - \frac{\partial \overline{u_i' u_j'}}{\partial x_j} \tag{2}$$

where u_i is the time velocity component, p is the pressure, ρ is the air density, ν is the kinematic viscosity, $\overline{u_i' u_j'}$ is the Reynolds stress term.

2.2.2. Turbulence modeling equations

In the present study, the Transition SST four-equation model was adopted as the turbulence model. This selection was justified by a systematic comparison of four CFD-applicable turbulence models: the Transition SST four-equation model, the S-A model, the k-omega model, and the k-epsilon model. Among these, the Transition SST four-equation model demonstrated superior simulation accuracy, forming the basis for its selection. The flow around the rotor blade involves complex hydrodynamic phenomena, and its Reynolds stress distribution has an important influence on the flow characteristics, so it is very important to select an appropriate turbulence model for accurate simulation. Although the traditional two equation model, such as k-epsilon and k-omega, has high computational efficiency, its applicability is limited under complex flow conditions. The k-omega model is widely used in the field of CFD because of its robustness and simple calculation u_{jm}. The model uses empirical damping function to deal with the flow near the wall, but the accuracy is often insufficient in the area of adverse pressure gradient, which limits its reliability in turbomachinery simulation [36].

In contrast, the k-omega model has better performance in the near wall region, and can accurately analyze the boundary layer characteristics without additional damping function, but its prediction ability is affected by free flow turbulence parameters. The transition SST model innovatively combines the advantages of the k-omega model in the near wall region with the stability of the k-omega model in the far field, and further introduces the transition prediction ability through the four equations framework, which significantly improves the simulation accuracy under complex flow conditions. The prediction ability of transition phenomenon is further strengthened, making it a better choice for simulating turbomachinery flow. Based on the above analysis, the transition SST four equation model was used to carry out the numerical simulation.

2.2.3. Turbine mathematical relations

The effectiveness of the rotor is determined by its power and torque. To quantify the aerodynamic performance of the fan, the following dimensionless parameters, torque coefficient and power coefficient, are introduced as follows:

$$C_p = \frac{P}{0.5\rho A v^3} \tag{3}$$

$$C_m = \frac{T}{0.5\rho A R v^2} \tag{4}$$

$$TSR = \frac{\omega R}{v} \tag{5}$$

where P is the output power, A is the swept area, D is the rotor diameter, H is the blade height and is the incoming wind speed, T is rotor torque and R is rotor radius, ω is the rotor angular velocity (rad/s).

2.2.4. Governing equations and turbulence model

This section will discuss the governing equations based on the existing simulations and the numerical settings in Ansys Fluent 2022R1.As a crucial step in numerical simulation, mesh generation can have an impact on the convergence rate and simulation accuracy. Quadrilateral structure grids are adopted to discretize the computational domain in all models as is shown in Fig. 2. The height of the first layer of the blade surface is set to $10^{-5}c$, to meet the requirements of the turbulence model for the solution process and guarantee that y^+ of the first node is less than 1.0. Three grids with different quantities are used to determine the appropriate number of grids required for calculation. The related parameters of the three grids are shown in Table 2.

Table 2. Grid specification.

Mesh density	Rough	Medium	Fine
Number of grid nodes on the blade	110	190	390
Number of grid nodes on the interface	100	160	320
Number of grid nodes at the inlet boundary	100	200	400
Averaged y+	1.2	0.9	0.87
The total number of grids	69782	153561	242315
Power coefficient	0.2615	0.2797	0.2802

The results reveal that the medium and the fine grid match well with the experiment results. Also, the deviation of the power factor between the medium and fine mesh is negligible. The medium grid is selected for the following simulation.

In order to verify the accuracy of the external flow field division, the wake in the downstream region of the rotor was studied by two-dimensional numerical simulation method. The two-dimensional computational fluid dynamics (CFD) method shows the ability of accurately simulating eddy current while reducing the computational cost. In order to ensure the stability of the upstream and downstream flow field of the rotor, the sensitivity analysis of two key design parameters was carried out in Fig. 3. The main purpose of this analysis is to minimize the impact of sidewall on turbine performance and flow device. The core parameters required for analysis include: "d" parameter indicates the distance from the rotor center to the outlet (range: 8D ~ 16D). The blockage rate is expressed as "d/w". After calculation, the blocking ratio is not more than 5%, which is within the allowable range. The data in the figure shows that as the outlet width do increases from 8D to 16D, the variation range of C_p value at different outlet distances is similar between 10D and 14D, and only small fluctuations are observed within this range. Based on the calculation results, d = 10D is recommended as the optimal choice.

2.2.5. Time step size study

At the same time, we also discussed the time step to determine the optimal time step in Table 3. We simulated the grid in the three different cases mentioned above under the horizontal grid, and obtained. In general, although the rough grid can maintain stability at all time steps (CFL number ≤ 5.49), it is not recommended because the grid is too coarse to accurately capture the details of the dimple vortex structure. In the medium grid, the time step of 0.00014544s is the best choice, and its CFL number is 4.82, which can achieve a balance between accuracy and computational efficiency, and can accurately capture the dimple vortex structure to meet the simulation demand of 30 cycles of rotation, while the 0.0001s step is more accurate but time-consuming, and the 0.0002s step is stable but less accurate. In the fine grid, the CFL number of 0.0001s step is 6.79, which is of high accuracy, but the calculation cost is too high. There is a risk of oscillation when the 0.0001 4544s step is close to the critical value, and the 0.0002s step is unreliable due to the excessive CFL number, which is not applicable.

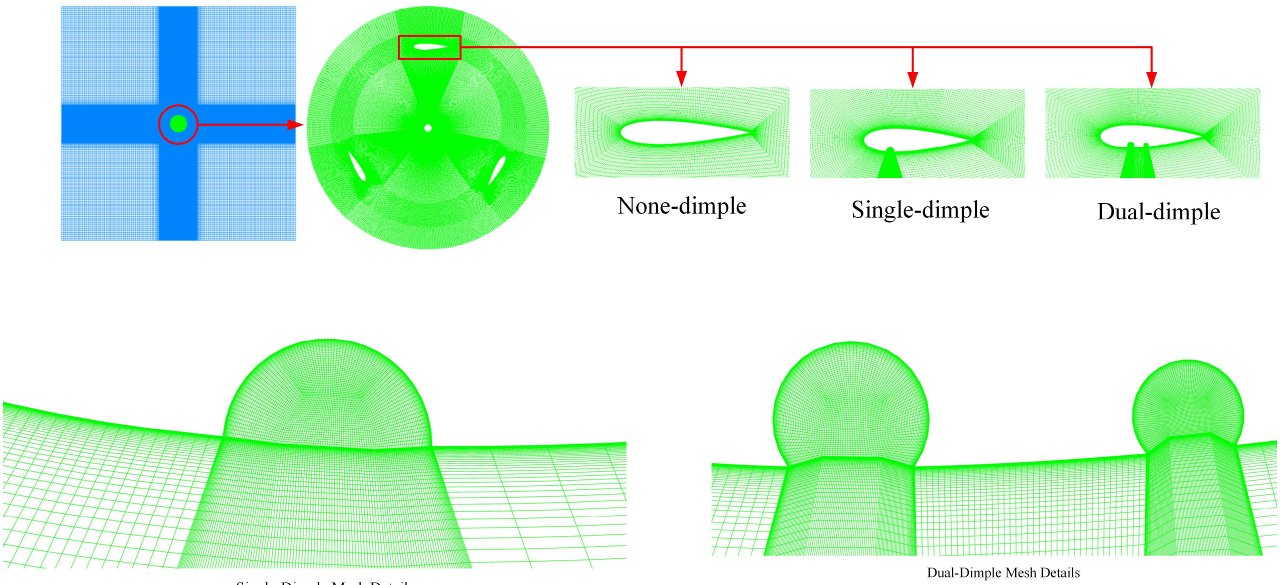

Fig. 2. Computational mesh and mesh details.

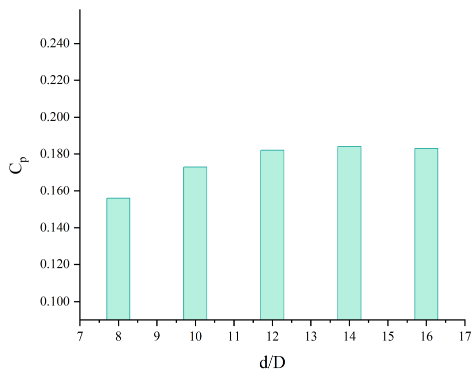

Fig. 3. Outlet distance effect.

Table 3. CFL number at different grid levels.

The quality of grids	Feature length (m)	Time step (s)	CFL
Rough	0.000364	0.0001	1.92
	0.000364	0.00014544	2.80
	0.000364	0.0002	3.84
Medium	0.000211	0.0001	3.32
	0.000211	0.00014544	4.82
	0.000211	0.0002	6.64
Fine	0.000103	0.0001	6.79
	0.000103	0.00014544	9.88
	0.000103	0.0002	13.59

Table 4. Level values of the Single-dimple airfoil.

Level	A Diameter	B Position	C Depth
1	0.24*c*	0.25*c*	+0.25*d*
2	0.08*c*	0.15*c*	0
3	0.16*c*	0.35*c*	-0.25*d*

2.3. Result validation

The SIMPLE algorithm and the second-order implicit transient format are used to solve the incompressible unsteady URANS equations. The equations of pressure, momentum, and turbulence were solved by second-order upwind space discretization [37]. The residual criterion is set to 10^{-5}. The number of rotating cycles of the wind turbine in all simulations is 30. As the monitoring parameters change periodically, the data of the last revolution will be investigated [39, 40]. The turbulence model is the Transition SST four-equation turbulence. As is shown in Fig. 4, the numerical simulation results are compared with the experimental results obtained by Danao [35] and the simulation results of Wekesa et al. [38]. When the *TSR* is in the range of 3 to 4, the simulation results are in good agreement with the experimental results. However, in the range of 4 to 5, there is a relatively large deviation between the simulation and experimental results. The predicted simulation value of the power coefficient is higher than the experimental results in this *TSR* range.

3. Orthogonal Experimental Design (OED)

OED is a research method to study multi-factor and multi-level test. Some representative points are chosen from the overall tests. And these selected points are evenly dispersed, neat, and comparable. Utilization of OED allows one to substantially reduce the number of tests and achieve the optimal solution based on restricted runs. In this paper, if all experiment combinations are simulated, it will take 5^6=15625 runs to find an optimal solution. However, it only needs a few of these combinations to determine the influence of each parameter on the blade using the OED method.

Firstly, we make a further discussion on the work of Sobhani [30]. It is concluded that although the dimple with a larger radius and closed position to the leading edge of the blade obtains better aerodynamic performance, optimal size is not clear. In this paper, a dimple is added to the inner side of the blade and three factors of dimple are chosen. Each factor has three levels, as shown in Table 4. And the positive and negative signs of the depth indicate that the center of the arc moves toward the inside and outside of the blade in the direction perpendicular to the chord line, respectively. As shown in Fig. 5, for example, if the center of arc ① moves inward by 0.25*d* (i.e., 0.5r), it will be recorded as +0.25*d*. Similarly, if the center of arc ② is located at the edge of the blade, it will be recorded as 0; if the center of arc ③ is moved outward by 0.25*d*, it will be recorded as -0.25*d*. The $L_9(3^4)$ orthogonal is used for the experimental design in Table 5. The working conditions in these orthogonal experiments are all calculated at the *TSR* of 3.

Table 5 shows that the influence of these three factors is ranged as follows: diameter, position, and depth. Besides, it can be seen that a larger size and more forward position of dimple are unlikely to always obtain better improvement. In particular, the single-dimple airfoil obtains the worse performance when the diameter of the dimple is up to 0.24*c*. However, the performance can be improved when the diameter of the dimple is 0.08*c*. The depth has the least influence among the three factors, and to a certain extent, the deeper dimple can bring a better performance.

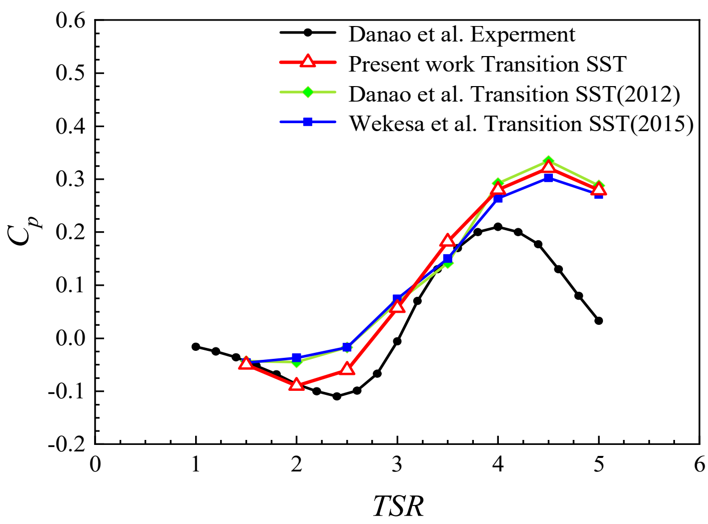

Fig. 4. Comparison between the CFD results and the experimental results.

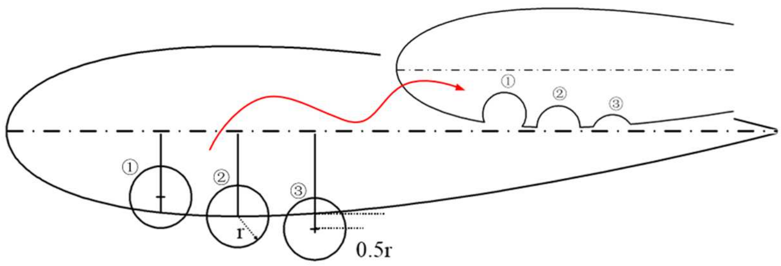

Fig. 5. Characteristics of the Single-dimple airfoil.

Table 5. The orthogonal test design.

Test number	A	Empty column	B	C	Test plan
1	1	1	1	1	A1B1C1
2	1	2	2	2	A1B2C2
3	1	3	3	3	A1B3C3
4	2	1	2	3	A2B2C3
5	2	2	3	1	A2B3C1
6	2	3	1	2	A2B1C2
7	3	1	3	2	A3B3C2
8	3	2	1	3	A3B1C3
9	3	3	2	1	A3B2C1
K1	0.088494	0.173298	0.215138	0.236786	
K2	0.242993	0.171584	0.191026	0.132067	
K3	0.139489	0.126093	0.064812	0.102124	
k1	0.029498	0.057766	0.071713	0.078929	
k2	0.080998	0.057195	0.063675	0.044022	
k3	0.046496	0.042031	0.021604	0.034041	
Range R	0.154499	0.047205	0.150325	0.134662	
Factors from primary to secondary			A B C		
Optimal plan			A2B1C1		

Table 6. Level values of the Dual-dimple airfoil.

Dimple 1			Dimple 2		
Diameter d_1	Depth l_1	Position x/c	Diameter d_2	Depth l_2	Distance s
0.07c	$+0.15d_1$	0.1	0.09c	$-0.3d_2$	0.2c
0.09c	$-0.15d_1$	0.2	0.05c	$-0.15d_2$	0.3c
0.13c	$+0.3d_1$	0.3	0.07c	0	0.35c
0.15c	$-0.3d_1$	0.4	0.11c	$+0.3d_2$	0.15c
0.11c	0	0.5	0.13c	$+0.15d_2$	0.25c

Table 7. Comparison of $l_{25}(5^6)$ orthogonal table and power coefficient.

Test number	Column number						Result	
	1	2	3	4	5	6	C_p	C_p/C_{p0}
1	0.07c	$-0.15d_1$	0.1c	0.09c	$-0.3d_2$	0.2c	0.078	135.05%
2	0.07c	$+0.15d_1$	0.2c	0.05c	$-0.15d_2$	0.3c	0.096	167.63%
3	0.07c	$+0.3d_1$	0.3c	0.07c	0	0.35c	0.104	181.40%
4	0.07c	$-0.3d_1$	0.4c	0.11c	$+0.3d_2$	0.15c	0.105	182.91%
5	0.07c	0	0.5c	0.13c	$+0.15d_2$	0.25c	0.093	162.53%
6	0.09c	$-0.15d_1$	0.2c	0.07c	$+0.3d_2$	0.25c	0.090	157.19%
7	0.09c	$+0.15d_1$	0.3c	0.11c	$+0.15d_2$	0.2c	0.111	192.25%
8	0.09c	$+0.3d_1$	0.4c	0.13c	$-0.3d_2$	0.3c	0.010	173.52%
9	0.09c	$-0.3d_1$	0.5c	0.09c	$-0.15d_2$	0.35c	0.084	146.32%
10	0.09c	0	0.1c	0.05c	0	0.15c	0.083	143.95%
11	0.13c	$-0.15d_1$	0.3c	0.13c	$-0.15d_2$	0.15c	0.086	149.26%
12	0.13c	$+0.15d_1$	0.4c	0.09c	0	0.25c	0.096	167.69%
13	0.13c	$+0.3d_1$	0.5c	0.05c	$+0.3d_2$	0.2c	0.112	194.04%
14	0.13c	$-0.3d_1$	0.1c	0.07c	$+0.15d_2$	0.3c	0.043	73.97%
15	0.13c	0	0.2c	0.11c	$-0.3d_2$	0.35c	0.070	122.05%
16	0.15c	$-0.15d_1$	0.4c	0.05c	$+0.15d_2$	0.35c	0.079	137.15%
17	0.15c	$+0.15d_1$	0.5c	0.07c	$-0.3d_2$	0.15c	0.095	165.46%
18	0.15c	$+0.3d_1$	0.1c	0.11c	$-0.15d_2$	0.25c	0.063	109.73%
19	0.15c	$-0.3d_1$	0.2c	0.13c	0	0.2c	0.060	104.55%
20	0.15c	0	0.3c	0.09c	$+0.3d_2$	0.3c	0.085	148.05%
21	0.11c	$-0.15d_1$	0.5c	0.11c	0	0.3c	0.058	100.36%
22	0.11c	$+0.15d_1$	0.1c	0.13c	$+0.3d_2$	0.35c	0.076	132.05%
23	0.11c	$+0.3d_1$	0.2c	0.09c	$+0.15d_2$	0.15c	0.098	170.50%
24	0.11c	$-0.3d_1$	0.3c	0.05c	$-0.3d_2$	0.25c	0.097	168.46%
25	0.11c	0	0.4c	0.07c	$-0.15d_2$	0.2c	0.093	160.95%

Table 8. OED results of the Dual-dimple airfoil.

	d_1	l_1	x/c	d_2	l_2	s
k1	0.095407	0.078097	0.068405	0.088285	0.087932	0.090499
k2	0.093533	0.094894	0.08303	0.093303	0.084407	0.076315
k3	0.081315	0.095368	0.096544	0.084992	0.080274	0.082691
k4	0.076477	0.077774	0.094567	0.081349	0.093649	0.0934
k5	0.084226	0.084826	0.088412	0.08303	0.084697	0.088055
max	0.095407	0.095368	0.096544	0.093303	0.093649	0.090499
min	0.076477	0.077774	0.068405	0.081349	0.080274	0.076315
average	0.086192	0.086192	0.086192	0.086192	0.086192	0.086192
R	0.094648	0.087969	0.140695	0.059768	0.066875	0.085427

According to the above data, adding a dimple on the blade can obtain good aerodynamic performance. Then, a dimple is added with different parameters behind dimple 1 in Fig. 6. The influential factors are set to 6, and the level of each influence factor is set to 5. These factors are the position *x/c*, diameter d_1, depth l_1 of dimple 1, diameter d_2, depth l_2 of dimple 2, and the distance *s* between the Dual dimples, respectively. Table 6 and Table 7 show the level of each factor and the distribution of the orthogonal table, respectively.

Our goal is to determine the optimal arrangement among the important design parameters. The range of parameters can be set in a relatively loose state. However, an excessively large size of dimple may damage the strength of the blade, and it hurts both dividing grids and calculating convergence. Therefore, the paper deals with the range of parameters in an acceptable range.

4. Results and Discussion

4.1. Analysis of the OED results

Section 4 begins with a systematic analysis of the impact of various design parameters on the power coefficient for dual-dimple arrangements, based on OED methodology as detailed in Section 4.1.

4.1.1. Analysis of the range of the OED results

The 25 working conditions are listed in Table 7 to identify the influence of design parameters. Table 8 lists the average power coefficient distribution as a function of different parameters and levels. R represents the range between the maximum and minimum values of a particular parameter at different levels. It is obvious that the position of dimple 1 has the largest R-value, which means that the factor of *x/c* has the greatest influence on the value of the power coefficient. The gray areas in Table 8 are the maximum values of each level. When the corresponding parameter of gray values adopts the maximum value, the value of the power coefficient is relatively high.

Table 8 shows that the weight of the influence of each parameter on the power coefficient is $x/c > d_1 > l_1 > s > l_2 > d_2$, and the corresponding level is k3, k1, k3, k1, k4, k2, respectively. According to the value range of the design parameters, the optimal solution is $d_1 = 0.07c$, $l_1 = +0.3d$, $x/c = 0.3$, $d_2 = 0.05c$, $l_2 = +0.3d$, $s = 0.15c$. The model of the optimal Dual-dimple airfoil as shown in Fig. 6. The C_p of the optimal Dual-dimple airfoil is 0.1227 for the numerical simulation at *TSR* = 3. The following numerical simulation adopts the model of the optimal Dual-dimple airfoil. At the same time, we also found that the 13th group had the worst effect, and the structure was shown as shown in the Fig. 7. .

4.1.2. Analysis of the variance of the OED results

Analysis of the variance is used to estimate the relative influence, each of which contributes to the power coefficient. It can reflect all the design parameters that have a different influential degree on the power coefficient.

Table 9 lists the results of variance and the parameters in the analysis process. The sum of squares of deviation specific to a design parameter is divided into the sum of squares within a group (SSW) and the sum of squares between groups (SSB) [40]. The degree of freedom within a group (*DoFW*) represents that the value of the total number of trials subtracts the number of levels, and the degree of freedom between groups (*DoFB*) represents that the value of the number of design parameter levels subtracts 1. Among them, F_{value} is determined by the following formula:

$$F_{value} = \frac{SSB/DoFB}{SSW/DoFW} \tag{6}$$

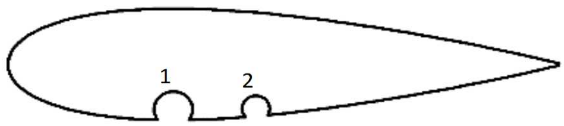

Fig. 6. Configuration of the optimal Dual-dimple airfoil.

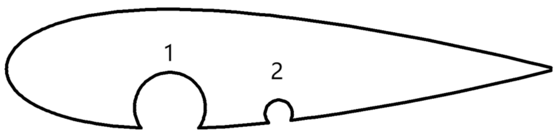

Fig. 7. The least effective blade structure.

Table 9. Variance table of OED analysis.

	d_1	l_1	x/c	d_2	l_2	s
SSW	0.005898	0.005711	0.004659	0.006753	0.006706	0.006283
SSB	0.001304	0.001491	0.002543	0.000449	0.000495	0.000919
DoFW	20	20	20	20	20	20
DoFB	4	4	4	4	4	4
F_{value}	1.105687	1.3054	2.729366	0.332587	0.369362	0.731342
$F_{0.1}$	2.25	2.25	2.25	2.25	2.25	2.25
Significance	0	0	1	0	0	0

The standard F_{value} is determined by the F table which provides the statistical significance. When DoFW is 20 and DoFB is 4, the standard F_{value} is 2.25 from the query table at the 10% significance level. When the F_{value} of a particular parameter is greater than the standard value F0.1, it means that the parameter has a significant effect on the power coefficient. In Table 9, the F_{value} of the position parameter x/c of arc 1 is 2.729366, which is greater than $F_{0.1}$. The F_{value} of other parameters is less than $F_{0.1}$. Therefore, the results of the analysis of variance revealed that the position parameter x/c of dimple 1 has the most influence on the aerodynamic performance, which is also consistent with the results of the orthogonal analysis.

The position x/c of dimples has the greatest impact on aerodynamic performance, which is directly related to the boundary layer and dynamic stall theory. In dynamic stall, insufficient kinetic energy in the boundary layer can lead to airflow separation, while the vortices generated by the dimples can replenish energy to the boundary layer to delay the separation. The location of the dimple determines the timing of the interaction between the vortex and the boundary layer: if it is too far forward, it will interfere with the incoming flow prematurely. If it is too late, the crucial stage of inhibitory separation will be missed. When x/c is at the optimal value, x/c = 0.3, the dimple can precisely inject energy when the boundary layer begins to weaken, effectively delaying dynamic stall. In contrast, parameters such as diameter and depth mainly affect the intensity of the eddy current, while the position parameter directly determines the spatiotemporal matching of the energy injection and separation process, and thus has the most significant impact.

In combination with the above, we also compared the orthogonal experiments of double dents, and quantitatively analyzed the lift coefficient Cl of smooth blade, optimal double dents blade (best) and worst double dents blade (worst) in Fig. 8. It can be seen that the peak lift coefficient of smooth blade is 2.02214, and the corresponding angle of attack is 17.6372°. The optimal double concave blade has a peak value of 2.27543, corresponding to an attack angle of 19.4646°, which is about 12.5% higher than that of the smooth blade, and a stall attack angle delay of 1.8274°, which has a significant advantage in the range of medium and high attack angles. For example, at 20°, it is about 26.4% higher than that of the smooth blade, and the peak resistance coefficient is reduced by about 36.3%, which has excellent comprehensive aerodynamic performance. The peak value of the worst double concave blade is about 1.6, which is about 20.9% lower than that of the smooth blade. The lift in the range of full angle of attack is low. It fluctuates violently at low angle of attack, and decreases faster at high angle of attack, which reflects the key influence of the concave layout parameters on the lift characteristics of the blade. Reasonable layout can significantly optimize the performance, otherwise it will reduce the performance.

4.2. Analysis of dimple influence

Figure 9 (a,b) compares the tangential and normal force coefficients of the Dual-dimple airfoil with those of the smooth airfoil at different azimuthal angles. A comparison of the tangential and normal force coefficients for smooth and Dual-dimple airfoils at different azimuths is shown in Fig. 9. It is easy to see that the Dual-dimple airfoil has a larger tangential and normal force coefficient than the smooth airfoil, and this variation is particularly dramatic around the 90~140° azimuth.

It can be observed in Fig. 9 (c) that the torque coefficient of both airfoils reaches their peak values at an azimuthal angle of around 90°. But compared with the smooth airfoil, the torque coefficient of the Dual-dimple airfoil has a higher peak and average value. And the downward trend of the Dual-dimple airfoil comes later than that of the smooth airfoil. Compared with the smooth airfoil, the torque coefficient and the normal force coefficient of the Dual-dimple airfoil obtain considerable improvement.

In Fig. 10, it introduces the lift coefficient with the changing angle of attack under different stages. The curve of both airfoils shows a similar trend. But the maximum value of the lift coefficient with the Dual-dimple airfoil is 2.275, which is greater than the smooth airfoil of 2.022. When the angle of attack is about 17°, the lift coefficient of the smooth airfoil reaches a stable level. However, the lift coefficient of the Dual-dimple airfoil continues to increase under a similar angle of attack. This discovery indicates that adding dimples on the blade is beneficial to delay the dynamic stall during the upstroke process.

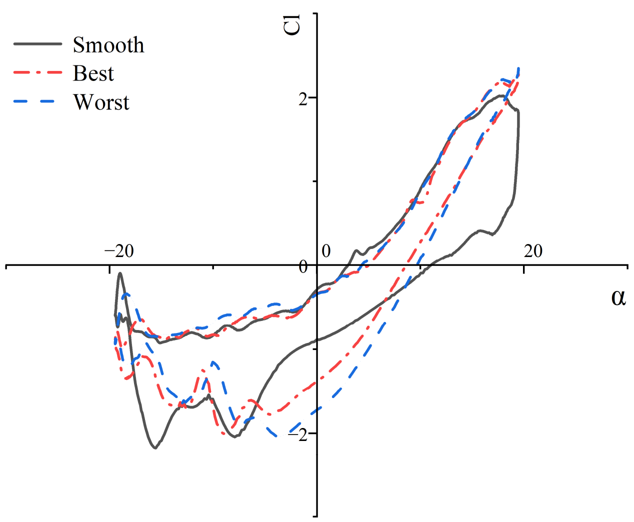

Fig. 8. Comparison of lift coefficient of smooth blade, best blade and worst blade.

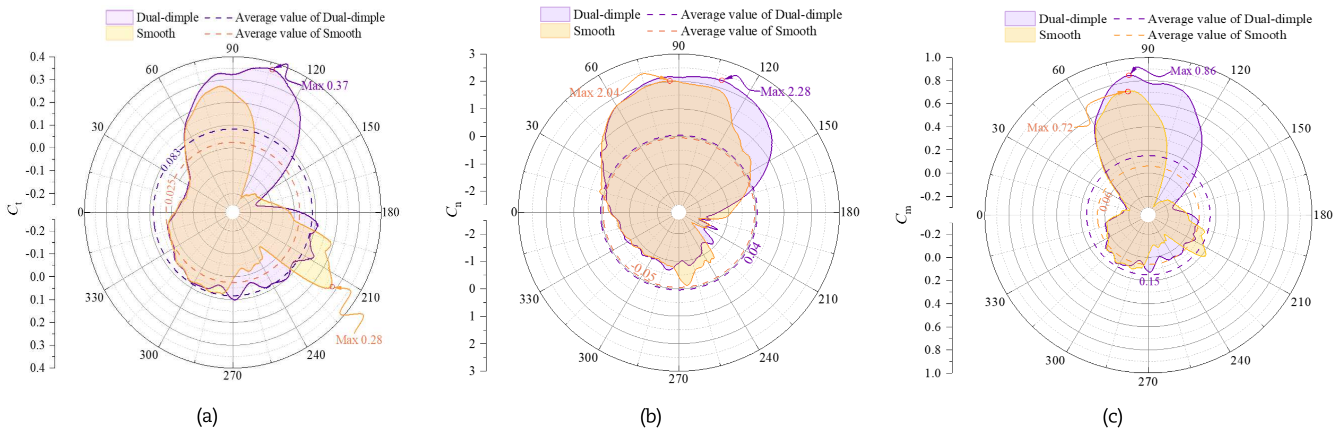

Fig. 9. Comparison of tangential/ normal force and torque coefficients of the smooth airfoil and the Dual-dimple airfoil, (a) Tangential force coefficient, (b) Normal force coefficient, (c) Torque coefficient.

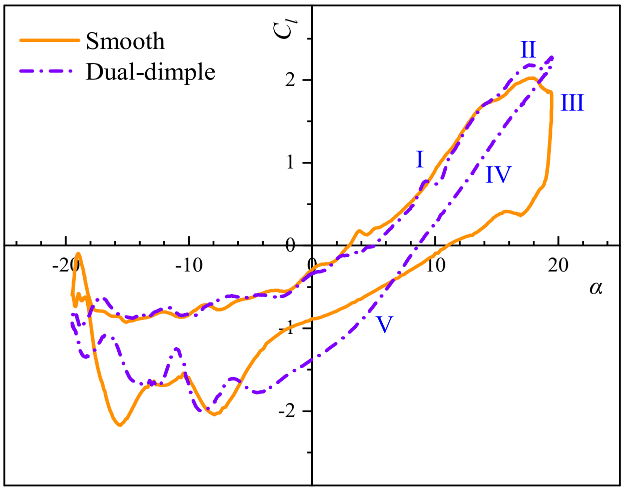

Fig. 10. Comparison of the lift coefficient of the smooth airfoil and the Dual-dimple airfoil.

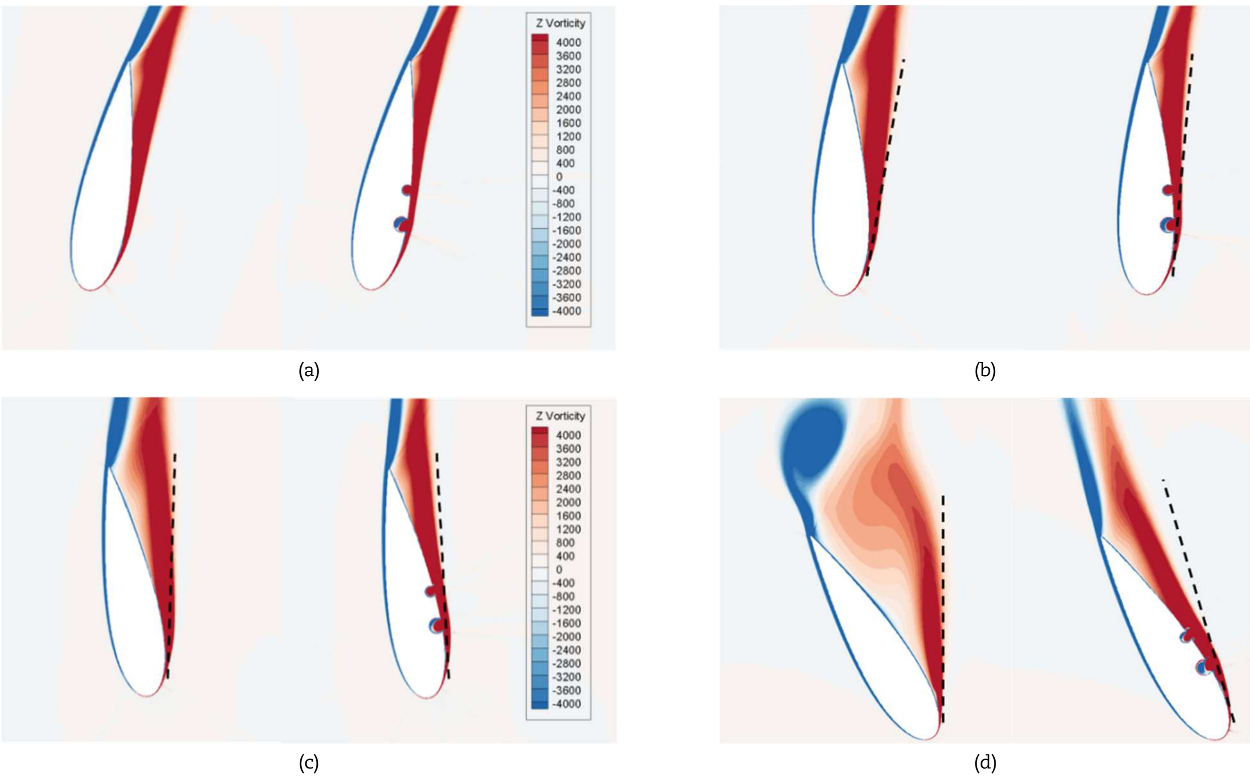

Fig. 11. Instantaneous contours of vorticity magnitude at TSR = 3, Azimuthal angle of 80°, Azimuthal angle of 90°, Azimuthal angle of 100°, Azimuthal angle of 120°.

There are several stages with the changing angle of attack in Fig. 8. In stage I, the lift coefficient of the smooth airfoil shows a gentle growth trend, while the lift coefficient of the Dual-dimple airfoil exhibits a high growth trend. This situation also reflects the differences between both airfoils. In stage II, the lift coefficient of the smooth airfoil also increases with a slow increase of angle of attack as in stage I, while the Dual-dimple airfoil curve is less volatile. With the angle of attack increasing slightly in stage III, the lift coefficient of both airfoils drops sharply in Fig. 10 due to the high-intensity eddy changes in the VAWT's system. Among both airfoils, the lift coefficient of the smooth airfoil decreases more quickly than that of the Dual-dimple airfoil. Furthermore, it can also be found that the torque exhibits the same trend as the lift coefficient.

After the maximum angle of attack is reached, the lift coefficient of both airfoils exhibits a trend of downward movement. In stage IV, the lift coefficient of the Dual-dimple airfoil is significantly higher than that of the smooth airfoil. It can be observed that the separation of the boundary layer is suppressed in Fig. 11 (at an azimuthal angle of 120°). In stage V, with the angle of attack moving towards a negative value, the lift coefficient of both airfoils decreases and becomes a negative value. Figure 11 shows the instantaneous contours of vorticity magnitude around the wind turbine. The separation of the vorticity happens in the boundary layer at an azimuthal angle of 90°. And the vorticity of the smooth airfoil separates a little faster than the Dual-dimple airfoil in Fig. 11 (d).

As Fig. 12 (a) shows the distribution of surface streamline at an azimuthal angle of 110° (it is close to the maximum angle of attack). When the separation point of the boundary layer with Dual-dimple airfoil leans back on the blade, the dynamic stall is delayed compared to the smooth airfoil. At this point, the smooth airfoil surface produces a large change in the vortex flow, so the vortex structure gets larger, and the lift coefficient drops sharply. Figure 12 (b) shows the enlarged surface streamline of the Dual-dimple. When the Dual-dimple airfoil runs to the current angle of attack, the vorticity produced from the Dual-dimple falls off on the blade. Compared with the smooth airfoil, the thickness of the boundary layer on the inner side of the Dual-dimple airfoil becomes thicker over time. It is because the shedding vortex rotated counterclockwise transfers energy to the boundary layer of the blade and inhibits the separation of the boundary layer. The Dual-dimple airfoil has a smaller vortex structure at the trailing edge of the blade compared to the Single-dimple airfoil.

In Fig. 13, there introduces the distribution of the pressure coefficient (C_{pe}) at an azimuthal angle of 110°. The pressure coefficient of the smooth blade drops sharply after reaching a peak at the leading edge and then shows a steady state along the blade, which is evidence of the greater degree of the separation of the boundary layer. However, the maximum value of the C_{pe} of the Single/Dual-dimple airfoils is higher than that of the smooth airfoil. The C_{pe} of the Dual-dimple airfoil presents obvious fluctuation, which is caused by the vortex produced by the dimple. Compared with the smooth airfoil, the C_{pe} of the Single/Dual-dimple airfoils generally decline gently. Although the C_{pe} of both airfoils shows a similar trend, the Dual-dimple airfoil exhibits better performance than that of the Single-dimple airfoil.

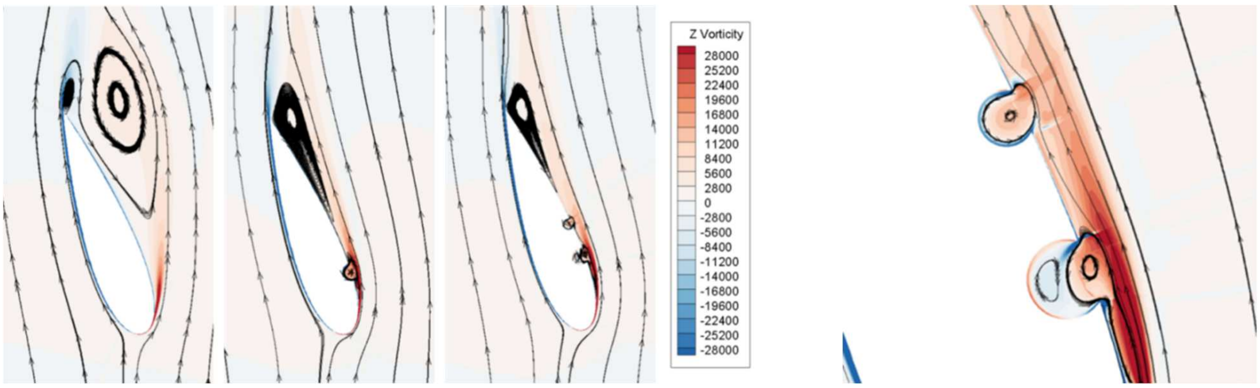

(a) (b)

Fig. 12. Surface streamline of three types of airfoils and partial enlargement at azimuthal angle of 110°, Surface streamline, Partial enlargement.

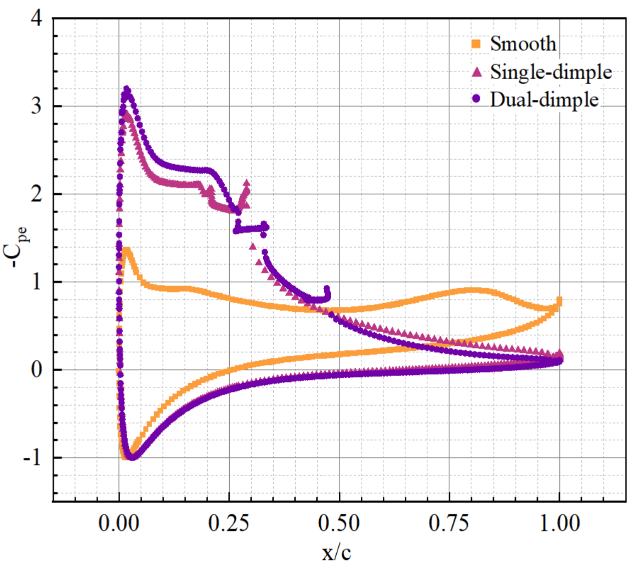

Fig. 13. Distribution of the pressure coefficient at an azimuthal angle of 110°.

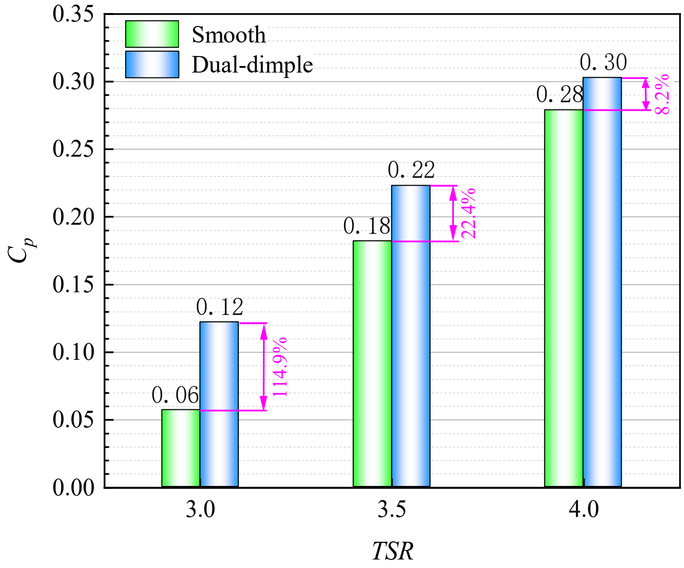

Fig. 14. Comparison of power coefficient between the Dual-dimple airfoil and the smooth airfoil.

As is shown in Fig. 14, the C_{pe} of the Dual-dimple airfoil is increased by 114.9%, 22.4%, and 8.2% at the *TSR* of 3, 3.5, and 4, respectively. Although the OED method is carried out at a *TSR* of 3, the performance of the Dual-dimple airfoil improves at other *TSR* as well. The phenomenon of the separation of the boundary layer directly illuminates the mechanism of the dynamic stall of the wind turbine. The results also reveal that the shedding vorticity formed by the airflow around the dimple flows to the bottom of the blade, and transfers energy to the blade's surface during the operation of VAWT. This phenomenon has a positive impact on suppressing the separation of the boundary layer and the efficiency.

5. Conclusion

This paper investigated the influence of the Dual-dimple airfoil on aerodynamic characteristics. Based on the OED method, the weight of influence on the C_{pe} was studied among the design parameters. Moreover, compared with the smooth airfoil, the airfoil with the optimal Dual-dimple layout was designed based on the weight of influence. From the results of the analysis, we can draw the following conclusions:

1) In this OED method, the position of dimple 1 represented the most influential important parameters, and its F_{value} is 2.729366. The F_{value} of other parameters is less than the standard F_{value} of 2.25.
2) The Dual-dimples with optimized parameters delayed the occurrence of a dynamic stall at a high angle of attack in the upstream stage. There was not much difference between the smooth airfoil and the Dual-dimple airfoil in the downstream stage.
3) The weight of the parameters on the C_{pe} was observed, the parameters with larger weight were concentrated in dimple 1, and the weight of the parameters on the C_{pe} lowers gradually in dimple 2. Therefore, the multiple dimples can further enhance the efficiency of VAWT. But this improvement became less significant as the number of dimples increased.
4) Compared with the smooth airfoil, the Dual-dimple airfoil has a higher C_{pe} by 114.9% at *TSR* of 3. And the value of the C_{pe} increases by 22.4% and 8.2% respectively at a *TSR* of 3.5 and 4. It is inferred that the impact of the dimple on the aerodynamic performance became less when the *TSR* gradually increases.

Regarding the research deficiencies and future prospects, the shortcomings lie in that we only studied the influence of single and double dimples on a specific NACA0022 airfoil VAWT, without exploring the effects of different airfoils or multiple dimples (three or more), and without verifying the numerical simulation results through experiments. For future prospects, we look forward to expanding to various airfoils and multiple dimple designs, combining wind tunnel experiments to verify the simulation conclusions, exploring the adaptability of dimples under variable wind speeds and variable tip speed ratios, and further enhancing the practical application value of VAWT.

Author Contributions

Y. Huang planned the scheme, developed the methodology, conducted validation and investigation, provided resources, wrote the original draft, handled software and visualization, performed formal analysis, and participated in review and editing; L. Zhang contributed to methodology, software, validation, investigation, and writing, acquired funding, and took charge of supervision and visualization; C. Song was involved in methodology, validation, investigation, and writing, and participated in supervision and visualization; G. Tong, Y. Zhao, T. Jiang, and X. Meng were responsible for supervision, validation, investigation, and visualization. The manuscript was written through the contribution of all authors. All authors discussed the results, reviewed, and approved the final version of the manuscript.

Acknowledgments

The authors would like to take this opportunity to sincerely thank the editor and reviewers for their prompt review and valuable comments, which have considerably improved the quality of this scientific contribution.

Conflict of Interest

The authors declared no potential conflicts of interest concerning the research, authorship, and publication of this article.

Funding

This research was funded by the Jilin Provincial Science and Technology Department of Science and Technology Key Research and Development Projects (Grant number 20210203210SF).

Data Availability Statements

The data that support the findings of this study are available on request from the corresponding author.

Nomenclature

C_{pe}	Pressure coefficient	*OED*	Orthogonal Experimental Design
SSW	Sum of squares within a group	*CFD*	Computational Fluid Dynamics
SSB	Sum of squares between groups	C_p	Power coefficient
DoFW	Degree of freedom within a group	*Re*	Reynolds number
DoFB	Degree of freedom between groups	*GF*	Gurney Flap
F_{value}	F-statistic	*WGD*	Wind Gathering Device
$F_{0.1}$	Critical F-value at 10% significance level	*LDCS*	Lift-Drag Combined Starter
TSR	Tip Speed Ratio	*VP*	Variable-Pitch
URANS	Unsteady Reynolds-Averaged Navier-Stokes method	*SB-VAWT*	Straight-Bladed Vertical Axis Wind Turbine
SST	Shear Stress Transport	*H-Darrieus*	H-type Darrieus wind turbine
D	The rotor diameter	*TSR*	Tip Speed Ratio
$d_{1,2}$	Diameter	c	The blade chord length
ds	The diameter of the center tower	σ	Solidity
$l_{1,2}$	Depth	x/c	Position
ρ	Fluid density	k	Turbulent Kinetic Energy

References

[1] Wang, M., Wang, C., Hnydiuk-Stefan, A., et al., Recent Progress on Reliability Analysis of Offshore Wind Turbine Support Structures Considering Digital Twin Solutions, *Ocean Engineering*, 232, 2021, 109168.
[2] Zhang, L., Li, Y., Zhang, H., et al., A Review of the Potential of District Heating System in Northern China, *Applied Thermal Engineering*, 188, 2021, 116605.
[3] Belloli, M., Bayati, I., Facchinetti, A., et al., A Hybrid Methodology for Wind Tunnel Testing of Floating Offshore Wind Turbines, *Ocean Engineering*, 210, 2020, 107592.
[4] Cheng, P., Huang, Y., Wan, D., A Numerical Model for Fully Coupled Aero-Hydrodynamic Analysis of Floating Offshore Wind Turbine, *Ocean Engineering*, 173, 2019, 183–196.
[5] Li, Q., Cai, C., Yasunari, K., et al., Prediction of Power Generation of Two 30kW Horizontal Axis Wind Turbines with Gaussian Model, *Energy*, 231, 2021, 121075.
[6] Maulana, Y.Y., Manshoor, B., Zaman, I., et al., Effect of Width and Height Ratio of Additional Savonius Blades on Darrieus' Vertical Axis Wind Turbine on Self-Ability Starting and Number of Turbine Revolutions, *Journal of Complex Flow*, 6(1), 2024, 6–10.
[7] Ahmad, M., Shahzad, A., Qadri, M.N.M., An Overview of Aerodynamic Performance Analysis of Vertical Axis Wind Turbines, *Energy & Environment*, 34(7), 2023, 2815–2857.
[8] Sharma, S., Sharma, R., Performance Improvement of Savonius Rotor Using Multiple Quarter Blades – A CFD Investigation, *Energy Conversion and Management*, 127, 2016, 43–54.
[9] Al - Gburi, K.A.H., Alnaimi, F.B.I., Al - Quraishi, B.A.J., et al., Enhancing Savonius Vertical Axis Wind Turbine Performance: A Comprehensive Approach with Numerical Analysis and Experimental Investigations, *Energies*, 16(10), 2023, 4204.
[10] Li Q, Maeda T, Kamada Y, et al. Investigation of Power Performance and Wake on a Straight-Bladed Vertical Axis Wind Turbine with Field Experiments, *Energy*, 141, 2017, 1113–1123.
[11] Shi, X., Sun, J., Zhong, S., et al., Flow Control of a Stalled S809 Airfoil Using an Oscillating Micro-Cylinder at Different Angles of Attack, *Renewable Energy*, 175, 2021, 405–414.
[12] Rezaeiha, A., Montazeri, H., Blocken, B., Characterization of Aerodynamic Performance of Vertical Axis Wind Turbines: Impact of Operational Parameters, *Energy Conversion and Management*, 169, 2018, 45–77.
[13] Zuo, W., Wang, D., Kang, S., Numerical Simulations on the Wake Effect of H-Type Vertical Axis Wind Turbines, *Energy*, 106, 2016, 691–700.
[14] Zhang, T., Wang, Z., Huang, W., et al., A Numerical Study on Choosing the Best Configuration of the Blade for Vertical Axis Wind Turbines, *Journal of Wind Engineering and Industrial Aerodynamics*, 201, 2020, 104162.
[15] Tang, G., Li, Y., Takao, K., et al., Effects of Blade Airfoil Chord Length and Rotor Diameter on Aerodynamic Performance of Straight-Bladed Vertical Axis Wind Turbines by Numerical Simulation, *Energy*, 253, 2022, 126325.
[16] Xu, B., Li, Z., Zhang, Z., et al., The Parametric Modeling and Two-Objective Optimal Design of a Downwind Blade, *Frontiers in Energy Research*, 9, 2021, 708230.
[17] Zhou, Z., Ding, W., Tong, W., et al., A Review: Approaches for Aerodynamic Performance Improvement of Lift-Type Vertical Axis Wind Turbine, *Sustainable Energy Technologies and Assessments*, 49, 2022, 101789.
[18] Jiang, R., Zhao, Z., Liu, H., et al., Numerical Study on the Influence of Vortex Generators on Wind Turbine Aerodynamic Performance Considering Rotational Effect, *Renewable Energy*, 196, 2022, 1269–1285.
[19] Li, Q., Takao, M., Kamada, Y., et al., Study on Stall Behavior of a Straight-Bladed Vertical Axis Wind Turbine with Numerical and Experimental Investigations, *Journal of Wind Engineering and Industrial Aerodynamics*, 164, 2017, 1–12.
[20] Zhen, Z., Si, Q., Wen, S., et al., Study on Variable Pitch Strategy in H - Type Wind Turbine Considering Effect of Small Angle of Attack, *Journal of Renewable and Sustainable Energy*, 9(5), 2017, 053302.
[21] Li, Y., Zhang, S., Takao, K., et al., Starting Performance Effect of a Truncated - Cone - Shaped Wind Gathering Device on Small - Scale Straight - Bladed Vertical Axis Wind Turbine, *Energy Conversion and Management*, 167, 2018, 70–80.
[22] Chen, C., Wang, L., Niu, M., Research on the Application of Improved NSGA - II in the Structure Design of Wind Turbine Blade Spar Cap, *Frontiers in Energy Research*, 11, 2023, 1160423.
[23] Zhang, M., Wang, G., Xu, J., Aerodynamic Control of Low - Reynolds - Number Airfoil with Leading - Edge Protuberances, *AIAA Journal*, 51(8), 2013, 1960–1971.
[24] Almohammadi, K., Ingham, D., Ma, L., et al., Modeling Dynamic Stall of a Straight Blade Vertical Axis Wind Turbine, *Journal of Fluids and Structures*, 57, 2015, 144–158.
[25] Zhang, T., Elsakka, M., Huang, W., et al., Winglet Design for Vertical Axis Wind Turbines Based on a Design of Experiment and CFD Approach, *Energy Conversion and Management*, 195, 2019, 712–726.
[26] Li, Y., Zhao, Y., Qu, C., et al., Aerodynamic Characteristics of Straight-bladed Vertical Axis Wind Turbine with a Curved-outline Wind Gathering

Device, *Energy Conversion and Management*, 203, 2020, 112249.
[27] Tayebi, A., Torabi, F., Flow Control Techniques to Improve the Aerodynamic Performance of Darrieus Vertical Axis Wind Turbines: A Critical Review, *Journal of Wind Engineering and Industrial Aerodynamics*, 252, 2024, 105820.
[28] Jiang, C., Zhao, P., Stoesser, T., et al., Experimental and Numerical Investigation of Twin Vertical Axis Wind Turbines with a Deflector, *Energy Conversion and Management*, 209, 2020, 112588.
[29] Feng, F., Tong, G., Ma, Y., et al., Numerical Simulation and Wind Tunnel Investigation on Static Characteristics of VAWT Rotor Starter with Lift - Drag Combined Structure, *Energies*, 14(19), 2021, 6167.
[30] Sobhani, E., Ghaffari, M., Maghrebi, M., Numerical Investigation of Dimple Effects on Darrieus Vertical Axis Wind Turbine, *Energy*, 133, 2017, 231–241.
[31] Yue, L., Pei, L., Hou, W., et al., Numerical Study of the Effect of Surface Grooves on the Aerodynamic Performance of a NACA4415 Airfoil for Small Wind Turbines, *Journal of Wind Engineering and Industrial Aerodynamics*, 206, 2020, 104263.
[32] Miladi, R., Jahanfar, K., Majid, N., et al., Performance Improvement of Darrieus Wind Turbine Using Different Cavity Layouts, *Energy Conversion and Management*, 246, 2021, 114693.
[33] Hosseini Rad, S., Ghafoorian, F., Taraghi, M., et al., A Systematic Study on the Aerodynamic Performance Enhancement in H-Type Darrieus Vertical Axis Wind Turbines Using Vortex Cavity Layouts and Deflectors, *Physics of Fluids*, 36(2), 2024, 025142.
[34] Ibrahim, A.A., Elbaz, A.M.R., Melani, P.F.A., et al., Power Augmentation of Darrieus Wind Turbine Blades Using Trapped Vortex Cavity, *Journal of Wind Engineering and Industrial Aerodynamics*, 223, 2022, 104949.
[35] Danao, L.A., Edwards, J., Eboibi, O., et al., A Numerical Investigation into the Influence of Unsteady Wind on the Performance and Aerodynamics of a Vertical Axis Wind Turbine, *Applied Energy*, 116, 2014, 111-124.
[36] Ghafoorian, F., Wan, H., Impact of Passive Modifications on the Efficiency of Darrieus Vertical Axis Wind Turbines Utilizing the Kline-Fogleman Blade Design at the Trailing Edge, *Energies*, 18(12), 2025, 2718.
[37] Menter, F.R., Review of the Shear-Stress Transport Turbulence Model Experience from an Industrial Perspective, *International Journal of Computational Fluid Dynamics*, 23(4), 2009, 305–316.
[38] Wekesa, D.W., Wang, C., Wei, Y., et al., A Numerical Analysis of Unsteady Inflow Wind for Site Specific Vertical Axis Wind Turbine: A Case Study for Marsabit and Garissa in Kenya, *Renewable Energy*, 76, 2015, 648–661.
[39] Rezaeiha, A., Kalkman, I., Blocken, B., CFD Simulation of a Vertical Axis Wind Turbine Operating at a Moderate Tip Speed Ratio: Guidelines for Minimum Domain Size and Azimuthal Increment, *Renewable Energy*, 107, 2017, 373–385.
[40] Arab, A., Javadi, M., Anbarsooz, M., et al., A Numerical Study on the Aerodynamic Performance and the Self-Starting Characteristics of a Darrieus Wind Turbine Considering Its Moment of Inertia, *Renewable Energy*, 107, 2017, 298–311.

ORCID iD

Yuewen Huang https://orcid.org/0009-0002-5677-8156
Lidong Zhang https://orcid.org/0000-0003-2975-460X
Changpeng Song https://orcid.org/0009-0004-7471-7765
Guoqiang Tong https://orcid.org/0000-0002-2924-1356
Yuze Zhao https://orcid.org/0009-0005-0247-2049
Tieliu Jiang https://orcid.org/0009-0001-7380-841X
Xin Meng https://orcid.org/0009-0005-3352-8295

How to cite this article: Huang Y., et al., Effects of Dimples as Vortex Cavities on the Aerodynamic Performance of Darrieus Vertical Axis Wind Turbine, *J. Appl. Comput. Mech.*, 12(3), 2026, 866-878. https://doi.org/10.22055/jacm.2025.48524.5295